Geophys. J. Int. (2003) **154,** 483–498

Modelling of seismic waves in heterogeneous media using a wavelet-based method: application to fault and subduction zones

Tae-Kyung Hong and B. L. N. Kennett

Research School of Earth Sciences, Institute of Advanced Studies, The Australian National University, Canberra, ACT 0200, *Australia.*
E-mails: tkhong@rses.anu.edu.au; brian@rses.anu.edu.au

Accepted 2003 March 5. Received 2003 March 3; in original form 2002 November 18.

SUMMARY

The wavelet approach to numerical simulation of elastic wave propagation is applied to models with localized heterogeneity, with significant contrasts with their surroundings. We consider zones with both lowered wave speed such as a fault gouge zone and elevated wave speeds such as in a subduction zone. In each of these situations the source lies within the heterogeneity. The representation of the source region has therefore been adapted to work directly in a heterogeneous environment, rather than using a locally homogeneous zone around the source. This extension also allows the wavelet method to be used with a wider variety of sources, e.g. propagating sources. For the fault zone we consider both point and propagating sources through a moment tensor representation and reveal significant trapped waves along the gouge zone as well as permanent displacements. For subduction zones a variety of effects are produced depending on the depth and position of the source relative to the subducting slab. A variety of secondary waves, such as reflected and interface waves, can be produced on wave trains at regional distances and tend to be more important for greater source depths.

Key words: elastic-wave theory, fault, heterogeneous media, numerical techniques, subduction zone, wavelets.

1 INTRODUCTION

Tectonic regions are associated with complex and faulted structures, which can bring material with considerable contrast in properties into close proximity. Earthquakes are initiated in regions of considerable heterogeneity, which needs to be taken into account in the description of the generation of seismic waves by the source. Small distortions in the wavefield associated with systematic structure can lead to substantial differences on further propagation (e.g. Li & Vidale 1996).

It is therefore necessary to develop techniques that can consider sources in a heterogeneous environment and that do not depend on the commonly used assumption of local homogeneity near the source (e.g. Alterman & Karal 1968; Kelly *et al.* 1976; Levander 1988). In many circumstances such an approximation can work well when waves propagate from a simple into a more complex zone (e.g. Yomogida & Etgen 1993), but may be misleading where the source region itself is complex.

Two representative regions in the Earth where tectonic processes develop strongly heterogeneous structures in which earthquakes initiate are fault and subduction zones. Many different styles of numerical techniques have been used to simulate the propagation of seismic waves in such regions. Finite-difference methods have been used in investigating trapped waves in fault zones (Li & Vidale 1996; Igel *et al.* 2002) and guided waves in a subduction zone with an accretionary prism (Shapiro *et al.* 2000). To study waveform and amplitude variations associated with subduction zones, Vidale (1987) applied a coupled finite-difference and Kirchhoff method, Furumura & Kennett (1998) implemented a pseudospectral method, and Cormier (1989) and Sekiguchi (1992) used Gaussian-beam methods.

Classical finite-difference techniques (e.g. Alterman & Karal 1968) generally need more gridpoints per wavelength than other methods implementing a high-accuracy differentiation scheme (e.g. the pseudospectral method). Since a large region needs to be considered for subduction zone modelling memory requirements are high. If strong heterogeneity needs to be modelled, numerical dispersion is likely (Hong & Kennett 2003). Higher-order finite-difference techniques (Igel *et al.* 1995; Falk *et al.* 1998) cure most of the limitations of classical finite-difference methods but require the source time functions to be smooth enough to be differentiated many times. This requirement makes it difficult to handle dislocation sources for which the displacement time functions are both complicated and may well not be differentiable.

The Gaussian-beam method is attractive because of its low computational cost for simple situations because it is built on the framework of ray theory, with the superposition of all Gaussian beams passing through the neighbourhood of a point. However, in zones of high heterogeneity the ray tracing itself becomes a daunting task. Furthermore, it is difficult to include all necessary secondary phases which may affect the waveforms, such as interface waves along a zone of contrast such as the boundary of a subducting slab.

Although a pseudospectral method (or Fourier method, Kosloff *et al.* 1984) can implement high-accuracy differentiation, the traction-free condition on a free surface is difficult to implement effectively. In the Chebyshev spectral method (Kosloff *et al.* 1990) the traction-free condition is satisfied using 1-D analysis at the boundary, but this method also suffers from a non-uniform spatial grid spacing in the vertical direction imposed from the character of the Chebyshev polynomials.

Recently, a wavelet-based method (WBM) has been introduced for modelling of elastic wave propagation (Hong & Kennett 2002a,b). Because the representation of differential operators is carried out to high accuracy, the WBM approach is very effective for describing propagation through highly heterogeneous random media, retaining both accuracy and stability (Hong & Kennett 2002c). In this paper we consider the extension of the WBM to a general source representation (such as dislocation sources) embedded in heterogeneous zones. The treatment of heterogeneity is based on splitting the second-order differential operators in the zone around the source into two parts, so that a simple first-order operator is all that is left at the source location itself.

The extended WBM scheme is applied to two representative problems with heterogeneous source regions: fault and subduction zones. Fault zones are composed of physically perturbed materials created during prior rupturing processes, and resultantly behave as low-velocity structures. In contrast, a subduction zone has a dynamically subducting cool slab that displays a high-velocity anomaly to surrounding media.

In the application to fault-zone problems, we probe the effects of trapped waves in the low-velocity fault zone and the permanent displacements around sources. We include dislocation sources (including a propagating rupture) in the fault zone and are able to include an arbitrarily complex time history of slip to handle the complexities of real events.

In modelling for subduction zones, we investigate waveform and amplitude variation of *SH* waves propagating through a subducting slab. The size of the subduction zone means that we need to take account of the sphericity of the Earth and we have to make the approximation of working in a cylindrical coordinate system for *SH* waves. Previous studies (e.g. Sekiguchi 1992) on waveform variation in subduction zones did not pay attention to effects of interface waves and post-critically reflected waves sufficiently in regional distances, we investigate those effects by varying the relative position of the source and the slab boundaries. In particular, since earthquakes are, in general, close to the boundaries of the subducting slabs (e.g. Pankow & Lay 2002), there are considerable possibilities for the development of interface waves that can travel considerable distances along the slab.

2 A WAVELET-BASED METHOD FOR ELASTIC WAVE MODELLING

In this section, we briefly introduce the wavelet-based method which is described more fully in Hong & Kennett (2002a,b).

The *P–SV* elastic wave equation system in 2-D including body force terms (f_x, f_z) and absorbing boundary conditions via attenuation factors (Q_x, Q_z) is given by

$$\frac{\partial^2 u_x}{\partial t^2} = -2Q_x\frac{\partial u_x}{\partial t} + \frac{1}{\rho}\left(\frac{\partial \sigma_{xx}}{\partial x} + \frac{\partial \sigma_{xz}}{\partial z} + f_x\right),$$
$$\frac{\partial^2 u_z}{\partial t^2} = -2Q_z\frac{\partial u_z}{\partial t} + \frac{1}{\rho}\left(\frac{\partial \sigma_{xz}}{\partial x} + \frac{\partial \sigma_{zz}}{\partial z} + f_z\right), \quad (1)$$

where (u_x, u_z) is the displacement vector and $(\sigma_{xx}, \sigma_{xz}, \sigma_{zz})$ are components of the stress tensor:

$$\sigma_{xx} = (\lambda + 2\mu)\frac{\partial u_x}{\partial x} + \lambda\frac{\partial u_z}{\partial z}, \quad \sigma_{zz} = \lambda\frac{\partial u_x}{\partial x} + (\lambda + 2\mu)\frac{\partial u_z}{\partial z},$$
$$\sigma_{xz} = \mu\left(\frac{\partial u_x}{\partial z} + \frac{\partial u_z}{\partial x}\right), \quad (2)$$

and $\lambda(x, z)$ and $\mu(x, z)$ are the Lamé coefficients. The attenuation factors $Q_j (j = x, z)$ control the dissipation rate of waves at the absorbing boundaries.

By introducing linear operators $(\mathcal{L}_{ij}, i, j = x, z)$ for spatial differential operators and recasting the governing equation system (1) in a displacement–velocity formulation, we obtain a set of first-order partial differential equations (PDEs) in time:

$$\frac{\partial u_x}{\partial t} = v_x, \quad \frac{\partial v_x}{\partial t} = -2Q_x v_x + \mathcal{L}_{xx}u_x + \mathcal{L}_{xz}u_z + \frac{f_x}{\rho},$$
$$\frac{\partial u_z}{\partial t} = v_z, \quad \frac{\partial v_z}{\partial t} = -2Q_z v_z + \mathcal{L}_{zx}u_x + \mathcal{L}_{zz}u_z + \frac{f_z}{\rho}, \quad (3)$$

where (v_x, v_z) is the velocity vector and the operators $\mathcal{L}_{ij}$ are given by

$$\mathcal{L}_{xx} = \frac{1}{\rho}\frac{\partial}{\partial x}\left[(\lambda + 2\mu)\frac{\partial}{\partial x}\right] + \frac{1}{\rho}\frac{\partial}{\partial z}\left(\mu\frac{\partial}{\partial z}\right),$$
$$\mathcal{L}_{xz} = \frac{1}{\rho}\frac{\partial}{\partial x}\left(\lambda\frac{\partial}{\partial z}\right) + \frac{1}{\rho}\frac{\partial}{\partial z}\left(\mu\frac{\partial}{\partial x}\right),$$
$$\mathcal{L}_{zx} = \frac{1}{\rho}\frac{\partial}{\partial x}\left(\mu\frac{\partial}{\partial z}\right) + \frac{1}{\rho}\frac{\partial}{\partial z}\left(\lambda\frac{\partial}{\partial x}\right),$$
$$\mathcal{L}_{zz} = \frac{1}{\rho}\frac{\partial}{\partial x}\left(\mu\frac{\partial}{\partial x}\right) + \frac{1}{\rho}\frac{\partial}{\partial z}\left[(\lambda + 2\mu)\frac{\partial}{\partial z}\right]. \quad (4)$$

The equation system (3) can be written as a form of first-order differential equation with a vector unknown $\mathbf{U}$:

$$\partial_t \mathbf{U} = \mathbf{L}\mathbf{U} + \mathbf{N}, \quad (5)$$

where $\mathbf{U}$ is $(u_x, v_x, u_z, v_z)^t$ and the operator matrix $\mathbf{L}$ is given by

$$\mathbf{L} = \begin{pmatrix} 0 & I & 0 & 0 \\ \mathcal{L}_{xx} & -2Q_x & \mathcal{L}_{xz} & 0 \\ 0 & 0 & 0 & I \\ \mathcal{L}_{zx} & 0 & \mathcal{L}_{zz} & -2Q_z \end{pmatrix}. \quad (6)$$

$\mathbf{N}$ is composed of the body forces $(0, f_x/\rho, 0, f_z/\rho)^t$. When additional boundary conditions are considered, such as traction-free conditions on a free surface or inside a medium (e.g. a medium with a cavity), these conditions can be expressed via equivalent forces using the stress values on the boundaries, added to the body force components in $\mathbf{N}$.

Spatial differentiations of displacement or velocity fields are conducted on wavelet spaces by projecting the differential operators and vector fields using a wavelet transform. The differentiated fields are recovered by recombining all the wavelet space contributions using an inverse wavelet transform. For more details, refer to Beylkin (1992) and Hong & Kennett (2002a,b).

With a semi-group approach (e.g. Beylkin & Keiser 1997), the discrete time solution of eq. (5) is given by

$$\mathbf{U}_{n+1} = \mathbf{U}_n + \delta t\mathbf{L}\mathbf{U}_n + \frac{\delta t^2}{2}\mathbf{L}^2\mathbf{U}_n + \cdots + \frac{\delta t^m}{m!}\mathbf{L}^m\mathbf{U}_n$$
$$+ \delta t\mathbf{N}_n + \frac{\delta t^2}{2}\mathbf{L}\mathbf{N}_n + \frac{\delta t^3}{6}\mathbf{L}^2\mathbf{N}_n + \cdots + \frac{\delta t^{m+1}}{(m+1)!}\mathbf{L}^m\mathbf{N}_n, \quad (7)$$

where δt is a discrete time step, $\mathbf{U}_n$ is the displacement–velocity vector at discrete time t_n, $\mathbf{N}_n$ is a vector of forcing terms and m controls the truncation order in the discrete time solution.

As we can see from eq. (7), this scheme needs multiple spatial differentiations on a delta function for a point force (e.g. $\mathbf{L}\mathbf{N}_n$), and numerical dispersion will occur if the matrix operator $\mathbf{L}$ is applied directly. This problem can be avoided if the source regions are assumed to be locally homogeneous, and linear operators are formulated in simplified forms where multiple first-order differentiations are replaced by a second-order differentiation (e.g. $\partial_x(a\ \partial_x u) \rightarrow a\ \partial_x^2 u$). So, the linear operators ($\mathcal{L}^s_{ij}$) in the source region are represented by

$$\mathcal{L}^s_{xx} = \frac{(\lambda_s + 2\mu_s)}{\rho}\frac{\partial^2}{\partial x^2} + \frac{\mu_s}{\rho}\frac{\partial^2}{\partial z^2},\quad \mathcal{L}^s_{xz} = \mathcal{L}^s_{zx} = \frac{(\lambda_s + \mu_s)}{\rho}\frac{\partial^2}{\partial x \partial z},$$
$$\mathcal{L}^s_{zz} = \frac{\mu_s}{\rho}\frac{\partial^2}{\partial x^2} + \frac{(\lambda_s + 2\mu_s)}{\rho}\frac{\partial^2}{\partial z^2}, \tag{8}$$

where λ_s and μ_s are values of the Lamé coefficients at the source position and $\mathcal{L}^s_{ij}$ are the components of the matrix operator ($\mathbf{L}_s$) in the source region. By applying this source-region scheme with $\mathbf{L}_s$ while the source is active, the WBM sustains numerical stability.

However, when a source is initiated in a heterogeneous region this approach is no longer valid and needs to be modified as discussed in the next section.

3 MODIFIED TECHNIQUE

3.1 Theory

We modify the source representation by using a linear combination of operators to cope with heterogeneity, whilst retaining numerical stability. We require that the operators both inside and outside the source zone should be equivalent to the linear operators $\mathcal{L}_{ij}$ in eq. (4) for a general medium. We extract the $\mathcal{L}^s_{ij}$ contribution in the source region, and write the new form of the linear operators $\mathcal{L}^r_{ij}$ as

$$\mathcal{L}^r_{xz} = \mathcal{L}_{xz},\quad \mathcal{L}^r_{xx} = \begin{cases} \mathcal{L}_{xx}, & z > z_s + l,\quad z < z_s - l, \\ \mathcal{L}^s_{xx} + \mathcal{L}^d_{xx}, & z_s - l \le z \le z_s + l, \end{cases}$$
$$\mathcal{L}^r_{zx} = \mathcal{L}_{zx},\quad \mathcal{L}^r_{zz} = \begin{cases} \mathcal{L}_{zz}, & x > x_s + l,\quad x < x_s - l, \\ \mathcal{L}^s_{zz} + \mathcal{L}^d_{zz}, & x_s - l \le x \le x_s + l, \end{cases} \tag{9}$$

where (x_s, z_s) is the source position and l defines the size of the immediate source zone. The additional operators $\mathcal{L}^d_{jj}(j = x, z)$ in a heterogeneous source zone take the form

$$\mathcal{L}^d_{xx} = \frac{1}{\rho}\frac{\partial}{\partial x}\left[(\Delta\lambda + 2\Delta\mu)\frac{\partial}{\partial x}\right] + \frac{1}{\rho}\frac{\partial}{\partial z}\left(\Delta\mu\frac{\partial}{\partial z}\right),$$
$$\mathcal{L}^d_{zz} = \frac{1}{\rho}\frac{\partial}{\partial x}\left(\Delta\mu\frac{\partial}{\partial x}\right) + \frac{1}{\rho}\frac{\partial}{\partial z}\left[(\Delta\lambda + 2\Delta\mu)\frac{\partial}{\partial z}\right], \tag{10}$$

where $\Delta\lambda(x, z) = \lambda(x, z) - \lambda_s$ and $\Delta\mu(x, z) = \mu(x, z) - \mu_s$.

It can be readily proved that $\mathcal{L}^s_{jj} + \mathcal{L}^d_{jj}$ is mathematically equivalent to $\mathcal{L}_{jj}$. Also, note that the terms $\mathcal{L}_{ij}(i \neq j)$ do not need to be recast in the new form since only multiple differentiations in the same direction (e.g. $\partial_x\partial_x$ or $\partial_z\partial_z$) develop numerical instability and they are not included in these operators. Therefore, the original form of $\mathcal{L}_{ij}$ can be implemented directly when $i \neq j$.

In addition, we can find that only the linear operators $\mathcal{L}^s_{ij}$ are needed at the source position since the Lamé coefficient difference terms ($\Delta\lambda$, $\Delta\mu$) vanish at this point. So, with this modified linear operators $\mathcal{L}^r_{ij}$, one can treat any variation in the properties of source regions without numerical dispersion.

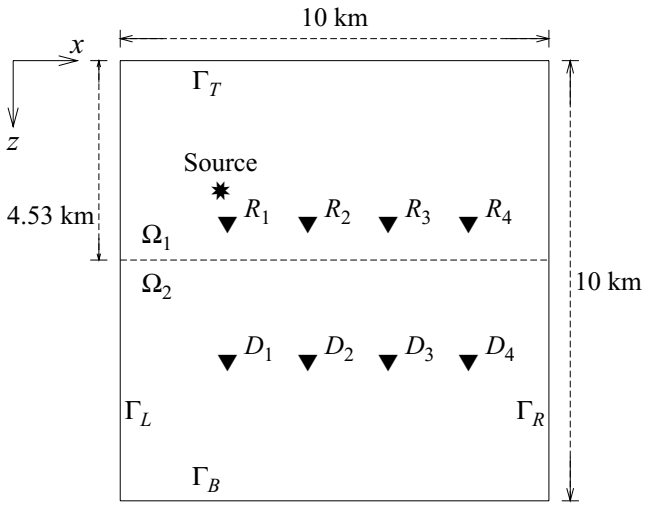

Figure 1. Representation of the two-layered medium used for the validation test of the modified WBM. The domain is 10×10 km^2 and a planar internal boundary is placed at a depth of $z = 4.53$ km. The compressional wave velocity (α_1) in the top layer (Ω_1) is 3.5 km s^{-1}, the shear wave velocity (β_1) is 2.0 km s^{-1}, and the density (ρ_1) is 2.2 Mg m^{-3}. The velocities in the bottom layer (Ω_2) are twice those in the top layer (i.e. $\alpha_2 = 7.0$ km s^{-1}, $\beta_2 = 4.0$ km s^{-1}) and the density (ρ_2) is 3.3 Mg m^{-3}. A vertically directed point source is applied at (2.34 km, 2.97 km), and four artificial boundaries (Γ_T, Γ_B, Γ_R, Γ_L) are treated by absorbing boundary conditions. In order to record time responses, eight receivers are deployed at depths of $z =$ 3.75 km (R_j, $j = 1, \ldots, 4$) and 6.88 km (D_j) from $x = 2.5$ km with a constant spacing of 1.875 km.

3.2 Validation test

In order to test whether the modified procedure is equivalent to the previous technique (Hong & Kennett 2002a,b), which has been validated by comparison with analytical solutions and other numerical methods, we compare the time responses of both techniques in a heterogeneous situation. We implement several values of l and compare the results to determine a suitable value for accurate and stable modelling and also to investigate whether any numerical anisotropy arises from the implementation of a combination of linear operators (see, e.g., Käser & Igel 2001).

We consider a two-layered medium (Fig. 1) in a 10×10 km^2 domain, represented by 128×128 gridpoints. The elastic wave velocities in the lower layer are twice those in the upper layer and the density ratio is a factor of 1.5. The four artificial boundaries (Γ_T, Γ_B, Γ_R, Γ_L) are treated via absorbing boundary conditions. A vertically directed point force is applied at (2.34 km, 2.97 km) inside the upper layer and eight receivers (R_j, D_j t $j = 1, \ldots, 4$) are deployed with a spacing of 1.875 km starting from $x = 2.5$ km at depths of $z = 3.75$ and 6.88 km. A Ricker wavelet with dominant frequency 4.5 Hz is introduced as the source time function.

When direct *P* and *S* waves are incident on an internal boundary, reflected (*PPr, PSr, SPr, SSr*) and transmitted (*PPt, PSt, SPt, SSt*) waves with phase coupling, interface waves and head waves develop and propagate from the boundary as indicated in Fig. 2.

We consider three different implementations of the modified approach with different values of l, and compare the resulting seismograms with those for the previous scheme. In case A we consider using the sum of the two operators $\mathcal{L}^s_{jj}$ and $\mathcal{L}^d_{jj}$ across the whole domain. In the other two cases we consider a more localized application of the split operator. In case B we use three grid steps for l, and in case C the extreme position where the modified technique

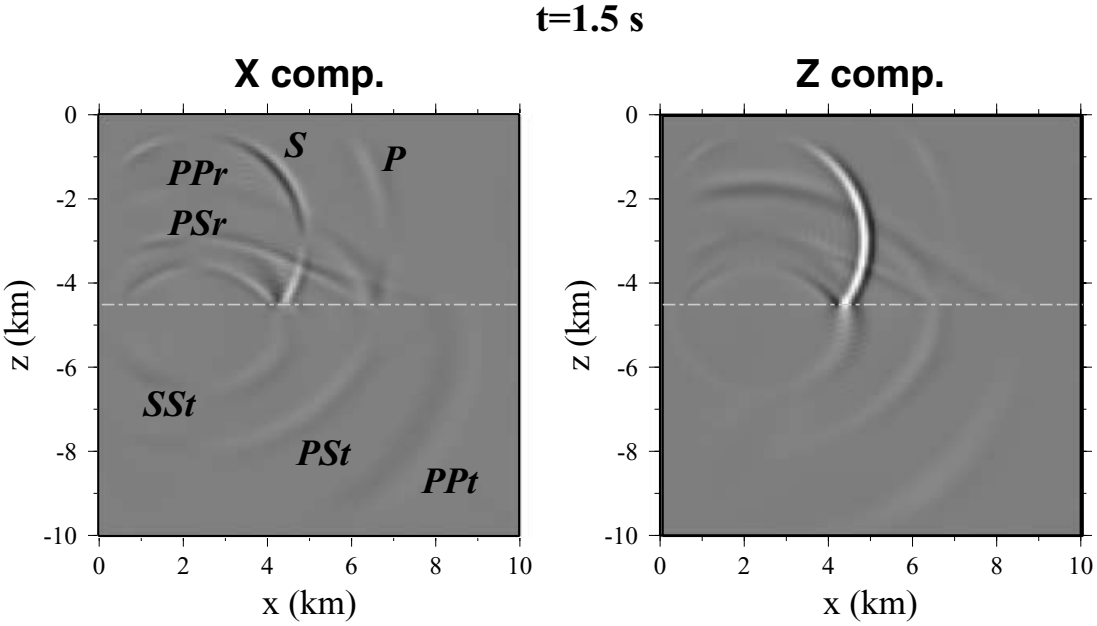

Figure 2. Snapshots of elastic wave propagation in the two-layered medium of Fig. 1 at $t = 1.5$s. Incident *P* and *S* waves are reflected (*PPr, PSr, SPr, SSr*) and transmitted (*PPt, PSt, SPt, SSt*) with phase coupling on the boundary.

is just the row and column of gridpoints in which the source are placed.

Fig. 3 displays a comparison of the numerical results for the three cases with reference solutions calculated using the previous approach. In general, the numerical results for cases A and B agree well with reference solutions for the whole wave trains except for a couple of slight misfits (indicated by the solid arrows in Fig. 3). These effects may arise from numerical anisotropy (e.g. Käser & Igel 2001), whereby the successive action of operators can have different effects depending on the order of application and analytically equivalent operators can have different numerical properties.

Although case C needs much less computational effort, the quality of the time response is not satisfactory. There are numerically dispersed phases arriving before the first-arrival phases and some slight misfits among the main phases (marked by broken arrows). The problem is that the operator is acting on too small a region to achieve accurate results. The quality of the time response can be ensured by applying the modified technique in a 'sufficiently broad localized' area, i.e. a band of rows and columns including a source position. Case B satisfies the number of gridpoints per wavelength needed for the WBM based on Daubechies-20 wavelets, i.e. three gridpoints (Hong & Kennett 2002a,b), and generates time responses that match well with the reference solutions.

Also, it is worth mentioning that the solutions, except for case A, display slight oscillations after main phases (see, *a* in the figure). This phenomenon is also related to numerical anisotropy, which develops through the transition of numerical schemes in limited areas. Here, note that the reference solutions are computed by the previous technique in Hong & Kennett (2002a,b), which needs both a source-region and a main-region scheme. In contrast, the case A displays good results. However, the maximum amplitude of the oscillations is less than 2 per cent of that of main phases and reduces with time, and thus the oscillations do not affect wavefields. In the following modelling, we implement the scheme for case A.

4 MODELLING IN FAULT ZONES

The implementation of a realistic fault source in numerical modelling has been a challenging issue, and many studies have confined their scope to cases using simple single-body forces (e.g. Huang *et al.* 1995; Igel *et al.* 2002). Although some *SH* studies based on finite-difference techniques (Vidale *et al.* 1985; Li & Vidale 1996) have managed to incorporate dislocation sources by considering near-field displacement fields with approximate analytic representations, such dislocation modelling is still difficult for *P–SV* waves. An attempt to incorporate dislocation sources in a *P–SV*-wave system by controlling stress values around a source position has been made by Coutant *et al.* (1995), but the proposed scheme is unsatisfactory for accurate modelling. Moreover, since a real fault zone is highly heterogeneous it is desirable to be able to implement dislocation sources, including rupture in realistic modelling.

The fault gouge zone has lowered velocities relative to its surroundings and so is able to support trapped waves. Such trapping phenomena have been investigated for fault zones by using 2-D (Li & Vidale 1996) and 3-D (Graves 1996) finite-difference codes or using analytic expressions (Ben-Zion 1998). The analytic expression for *SH*-type fault-zone trapped waves with a unit source in a uniform zone have been established by several studies (e.g. Li 1988; Ben-Zion & Aki 1990; Li & Leary 1990; Li *et al.* 1990). They demonstrated shear waveform variations for 2-D fault zones as a function of the parameters of the fault zone and the observation pattern, e.g. fault-zone width, velocity structures, relative source and receiver positions, and attenuation factors; they were able to show clear development of trapped waves and head waves as features of time responses in fault zones. The analytical approach demonstrates the presence of the phenomenon but is not able to handle heterogeneity or more complex geometry. Such effects can, however, be examined with numerical methods such as the higher-order finite-difference technique (e.g. Jahnke *et al.* 2002), and they could treat a problem with seismic-wave initiation on a

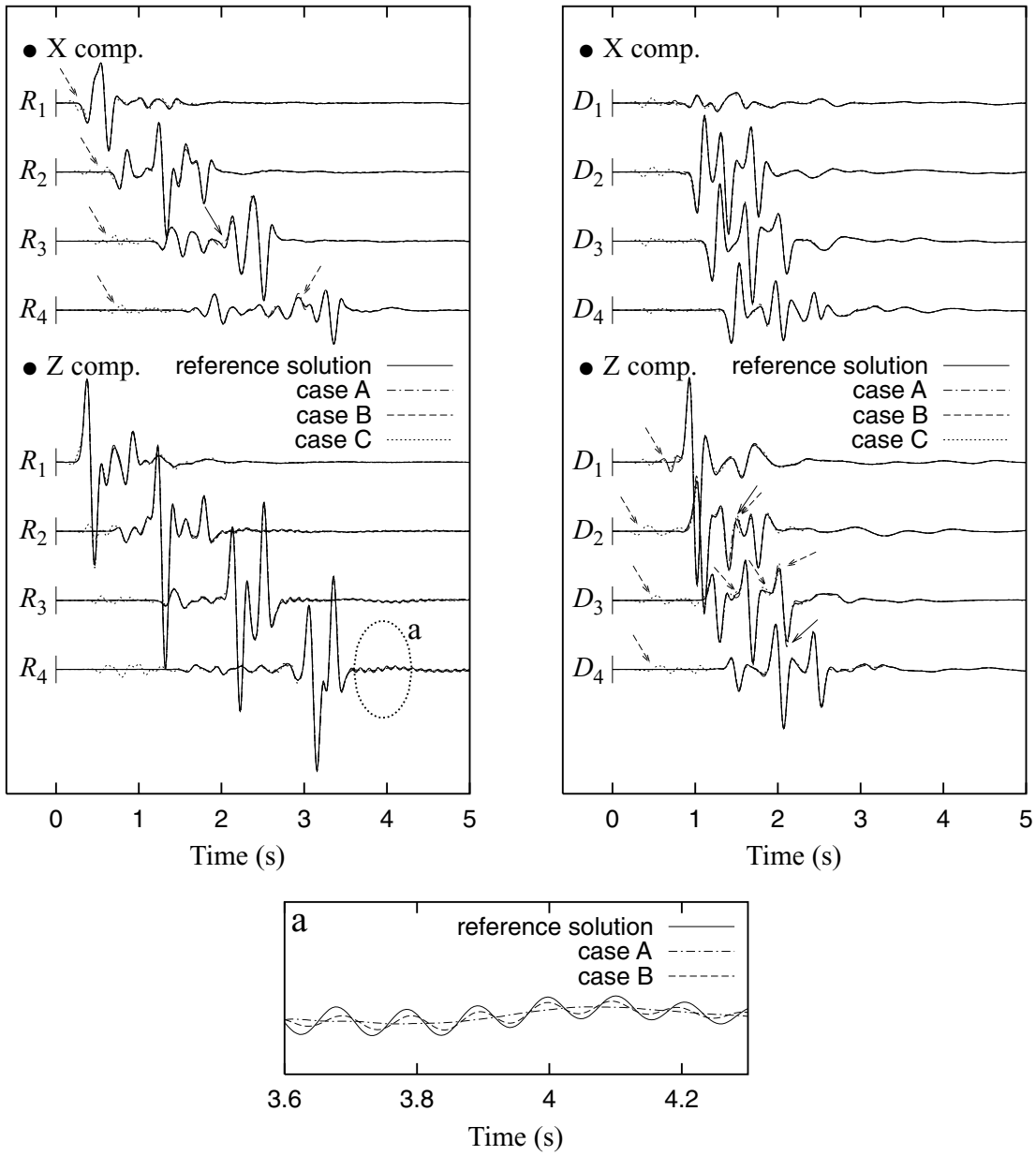

Figure 3. Comparisons of time responses, for several different versions of the modified WBM with a reference solution by the previous method (Hong & Kennett 2002b). The seismograms are recorded at eight receivers (R_j, D_j, $j = 1, \ldots, 4$) in Fig. 1. Amplified seismograms are provided for those of vertical component in R_4 (marked a). Case A applies the modified WBM technique to the whole domain, case B to a region three gridpoints across around the source point, and case C to a row and a column of gridpoints including a source position. Major misfits in the waveforms for case C are indicated by broken arrows, with solid arrows for other cases. The discrepancies for case C mainly arise from numerical dispersion. Records of D_j are amplified by a factor of the order of 6 for display.

material boundary in a fault zone. However, the finite-difference scheme may generate artificially attenuated seismic waves in media with complex strong heterogeneities (Hong & Kennett 2003) and has difficulty in treating a complex (unsmooth) source time function. The WBM is particularly effective in this context because of its capacity to handle strong heterogeneity, and, as we shall see, is able to include a propagating rupture with a rough source time function within the heterogeneous zone. Note that the WBM has been shown to preserve the energy of seismic waves correctly even in strongly perturbed media (Hong & Kennett 2003).

4.1 Implementation of dislocation sources

Dislocation sources can be implemented in the WBM through the double-couple force system based on a moment-tensor ($\boldsymbol{M}$) representation, and the equivalent body force $\mathbf{f}(t)$ for the dislocation sources can be expressed as (e.g. Ben-Menahem & Singh 1981; Komatitsch & Tromp 2002)

$$\mathbf{f}(t) = -\boldsymbol{M} \cdot \nabla \delta(\mathbf{r} - \mathbf{r}_s) D(t), \tag{11}$$

where $D(t)$ is the displacement history of a particle on the fault, $\mathbf{r}$ is the location vector and $\mathbf{r}_s$ is the location of the source, (x_s, z_s).

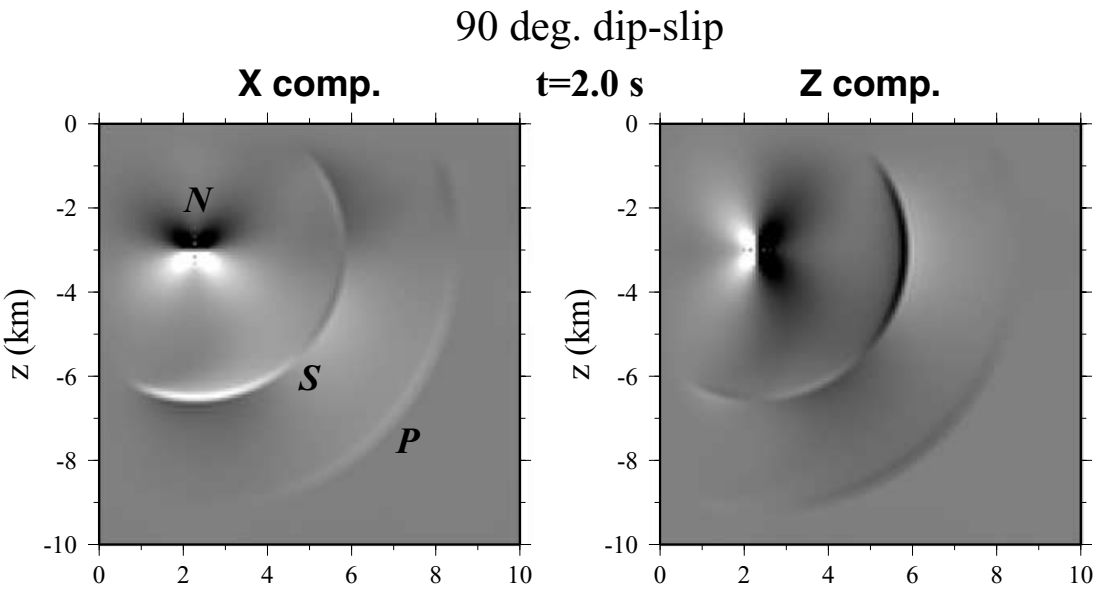

Figure 4. Snapshots of elastic wave propagation from a 90° dip-slip fault in a homogeneous medium. Both permanent displacements (*N*) and transient wavefields (*P*, *S*) are clearly shown.

Note that $\dot{D}(t)$ corresponds to the far-field source time function and the area under $\dot{D}(t)$ is unity (Vidale *et al.* 1985; Lay & Wallace 1995).

For an arbitrary fault the moment tensor can be expressed in terms of strike angle (ϕ), dip angle (ξ) and rake angle (η) of a fault geometry (e.g. Lay & Wallace 1995; Kennett 2001). the strike angle (ϕ) is measured from the north, the dip angle (ξ) from the horizontal plane normal to z direction and the rake angle (η) from the strike direction on the fault plane.

We consider a thrust (90° dip-slip) fault, which is placed parallel to the E–W direction and the corresponding moment tensors can be computed easily for the geographic reference frame (see, e.g., Lay & Wallace 1995, p. 343; Kennett 2001, p. 72). With the assumption that there is no structural variation in the y-direction, the thrust fault source can be implemented in 2-D as a 90°dip-slip fault activated on a vertical plane (x–z plane). Here, x corresponds to east and z is the downward vertical direction. The results for this line source in 2-D can be adjusted to match the geometrical spreading in 3-D for a point source by convolving seismograms with $1/\sqrt{t}$ and differentiating in time (Vidale *et al.* 1985; Igel *et al.* 2002).

Fig. 4 displays snapshots of elastic wave propagation in a homogeneous medium ($\alpha = 3.15$ km s^{-1}, $\beta = 1.8$ km s^{-1}, $\rho = 2.2$ Mg m^{-3}) with 90°dip-slip on a fault plane. Here a ramp excitation model where a fault slip increases linearly with time during the slip duration time (t_r), is considered for the displacement time function $D(t)$; we take 0.1 s for t_r in this study. Permanent displacements induced by the dislocation are found in a four-lobed pattern around the source position (*N* in Fig. 4), and diminish with distance as r^{-1}. On the other hand, a transient displacement activated by propagating elastic waves falls off with distance as $1/\sqrt{r}$ (Vidale *et al.* 1985). Therefore, in the far field, only the transient displacements are discernible in wavefields.

We are able to simulate the effect of rupture propagation by combining several dislocation sources with their own source time histories, and model a simple rupture problem using a ramp source time function in Section 4.3.

4.2 Modelling with a point dislocation in a fault zone

We consider a model of a fault gouge zone with significant heterogeneity in a material with lower wave speeds than its surroundings and simulate the response from a dislocation source in the fault zone. A horizontal fault zone (Ω_1 in Fig. 5) with random

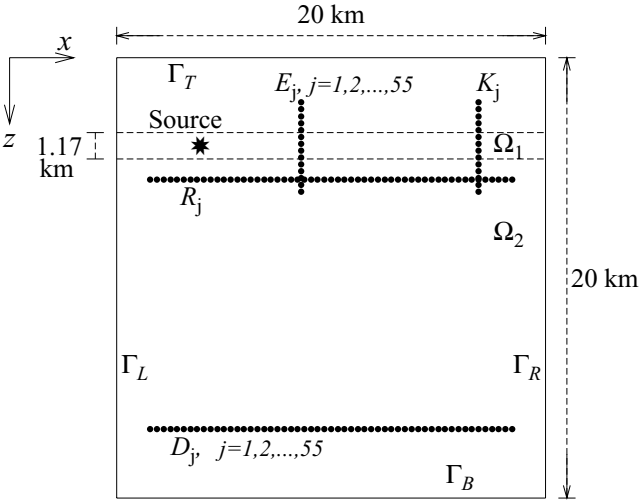

Figure 5. Representation of a domain (20 ×20 km^2) with a perturbed fault zone. The average compressional wave velocity (α_1) in the fault zone (Ω_1) is 2.63 km s^{-1}, the shear wave velocity (β_1) is 1.5 km s^{-1}, and the density (ρ_1) is 1.83 Mg m^{-3}. The velocities in the background medium (Ω_2) are 3.15 km s^{-1} for P(α_2), 1.8 km s^{-1} for S waves (β_2), and the density (ρ_2) is 2.2 Mg m^{-3}. The perturbation of the fault zone is represented through a stochastic process such that physical parameters are randomly perturbed with standard deviations of 10 per cent for the wave velocities and 8 per cent for the density. A 90°dip-slip dislocation source is applied at (3.9 km, 4.0 km), and four artificial boundaries (Γ_T, Γ_B, Γ_R, Γ_L) are treated by absorbing boundary conditions. 220 receivers are deployed at $z = 5.5$km (R_j, $j = 1, 2, \ldots, 55$), $z = 16.9$ km (D_j), $x = 8.59$ km (E_j) and $x = 16.9$ km (K_j) with a constant spacing.

perturbation in physical properties (wave velocities, density) is set in a homogeneous background medium (Ω_2) where the *P*-wave velocity (α_2) is 3.5 km s^{-1}, the *S*-wave velocity (β_2) is 2.0 km s^{-1} and the density (ρ_2) is 2.2 Mg m^{-3}. The average wave velocities in the fault zone are 2.63 km s^{-1} for *P* waves (α_1) and 1.5 km s^{-1} for *S* waves (β_1), and the average density (ρ_1) is 1.83 Mg m^{-3}. A 90°dip-slip dislocation source is located in the middle of the fault zone at $x = 3.9$ km, $z = 4.0$ km. The thickness of the fault zone is 1.17 km and the perturbations in the zone are generated from a stochastic representation using a von Karman autocorrelation function (*cf.* Sato & Fehler 1998) with Hurst number 0.25 and correlation distance 56 m. The wave velocities in the zone have a 10 per cent standard deviation and the density 8 per cent. More detailed information on the construction of suitable stochastic media has been discussed in previous studies of Hong & Kennett (2003) and Roth & Korn (1993).

Fig. 6 displays snapshots of elastic wave propagation in the medium with the fault zone, at $t = 3.5$ and 9.5 s. Various reflected waves develop inside the fault zone, and parts of the multireflected waves drain continuously into the homogeneous background medium following after direct phases (*P*, *S* in the figure). In particular, the *P* waves generated inside the fault zone give rise to a multiplicity of *SV* head waves. Meanwhile, most of the *S* waves are trapped in the low-velocity layer in the form of overcritically reflected waves, and so significant energy is transported along the layer (*T* in the figure) at a fairly slow group speed. The trapped waves on the vertical component are much larger than those on the horizontal component; this arises from the combination of the fault zone geometry (i.e. horizontal extension) and slip direction of the fault (i.e. 90° dip-slip).

The equivalent 3-D time response for two sets of 110 receivers at 313 m spacing, placed at depths of $z = 5.5$ and 16.9 km, are shown in Fig. 7. The upper set of receivers is set close to the fault zone and so emphasizes near-field effects, whilst the lower set is dominantly influenced by the far-field radiation. The onsets of the *P* arrivals are relatively simple because they come in ahead of any of

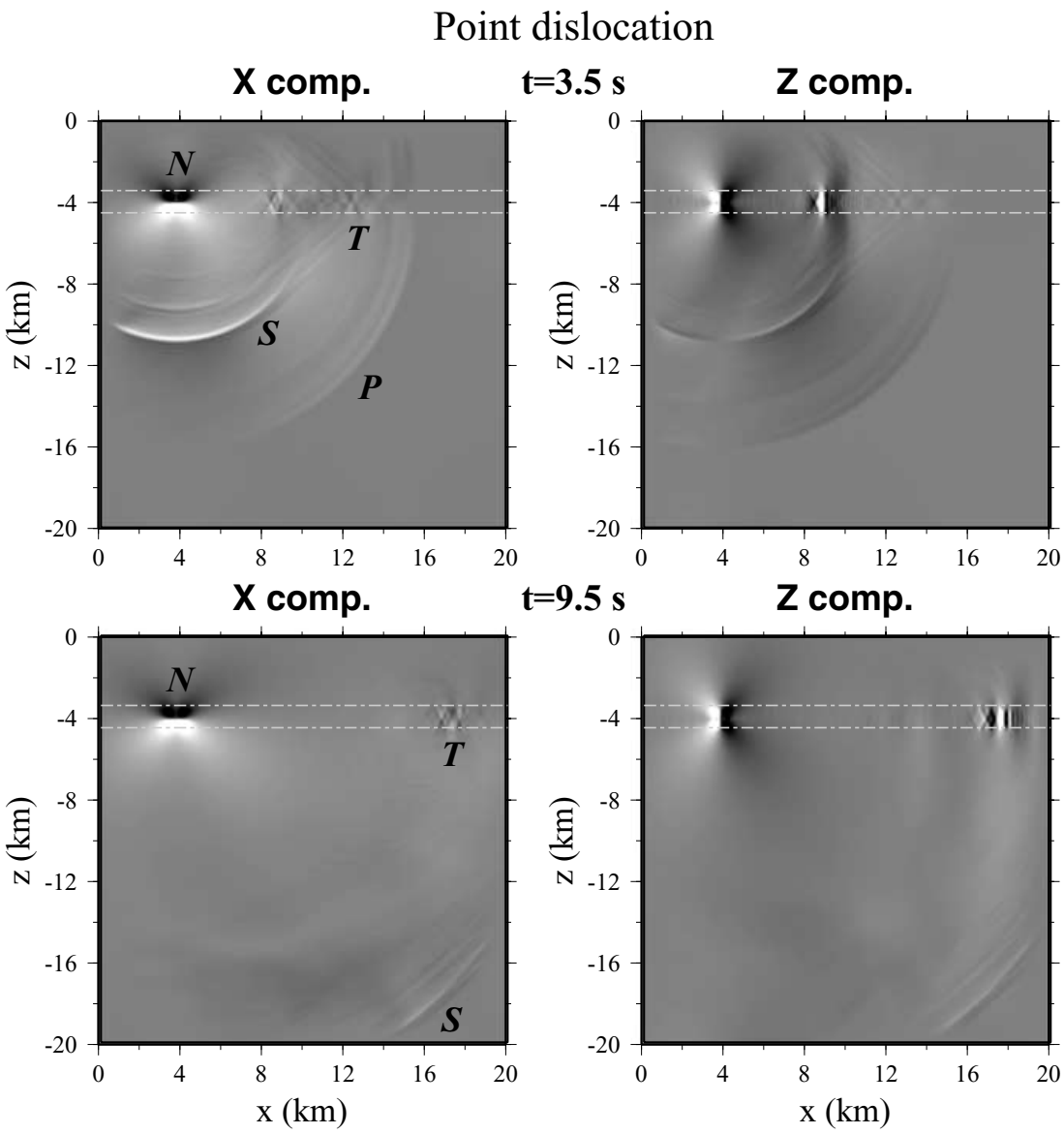

Figure 6. Snapshots of elastic wave propagation in the medium with a horizontal fault zone (see Fig. 5) with a 90°dip-slip dislocation source. Multireflected phases follow after direct phases (*P* and *S* in the figure) from the source. Also considerable trapped waves (*T*) develop inside the fault zone.

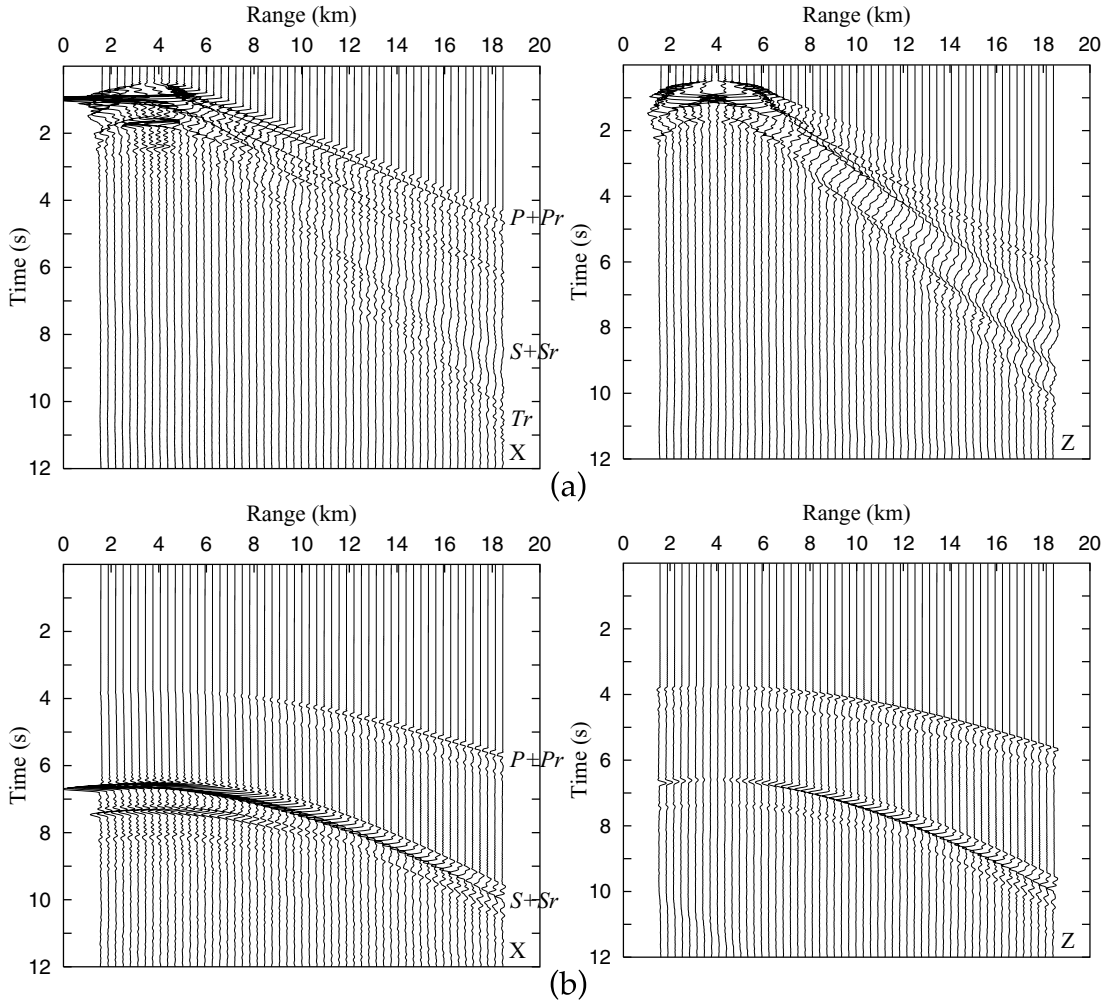

Figure 7. Time responses, with conversion to a 3-D response, at 110 receivers placed at (a) depth $z = 5.5$ (R_j in Fig. 5) and (b) 16.9 km (D_j) with an appropriate conversion procedure to the case of a point source. Multireflected phases (*Pr, Sr*) in a fault zone follow direct waves (*P, S*). Trapped waves interfere with random heterogeneities in the fault zone, and leak into the background medium in a form of scattered waves (*Tr*).

the scattered arrivals, but the influence of the heterogeneity is seen in the significant *S* arrivals for the *x* component on the upper line of receivers. The main trapped wave is of relatively low frequency, reflecting evanescent decay outside the fault-zone waveguide, but is accompanied by a higher-frequency coda with complex waveforms from multiple scattering in the fault zone (*Tr* in the figure). A distinct complex of scattered energy is seen on the *x*-component seismograms for small offsets from the source location. At larger distances a more coherent set of arrivals follows *S* and becomes more distinct for larger offsets.

The nature of the trapped wave phenomena can be most clearly seen in a receiver profile across the fault zone as illustrated in Fig. 8. The lines are set at 4.7 and 13.0 km from the source. On the closer profile, Fig. 8(a), there is still a significant influence from near-field effects and the main part of the trapped wave train tends to merge with the direct phases. The heterogeneity in the gouge zone leads to an extended coda of backscattered waves on the *z* component. On the further line, Fig. 8(b), the nature of the trapping phenomena becomes more evident. On the *x* component the fast *P* waves in the surrounding material link into the slower *P* waves in the gouge from which a significant *SV* head wave is being shed. The main amplitude on the *z* component lies as expected in the *S* wave and decays exponentially away from the fault zone so that relatively low-frequency energy dominates at the receivers furthest from the fault zone, and a similar pattern was reported in Li & Leary (1990, Figs 7 and 8). Part of the trapped waves consists of conversions between *P* and *S* and these are again prominent on the *z* component. The patterns of arrivals including long dispersed wave trains behind *S* are similar to those recorded from aftershocks of the Hector Mine earthquake in California (Li *et al.* 2002) in a similar profile across the fault zone. In this case the concentration of high-frequency arrivals was used as a means of mapping out the location of the fault zone.

4.3 Modelling with rupture propagation

In studies of ground motion in the vicinity of earthquakes it is normally not adequate to approximate fault sources by a point dislocation source since the radiation patterns and frequency content of the transient waves are strongly dependent not only on fault geometry but also on the dynamic source process. For instance, Kasahara (1981) showed that radiation patterns vary with the ratio of rupture velocity to shear wave velocity in the background medium and they are shown to be elongated with an increase of rupture velocity.

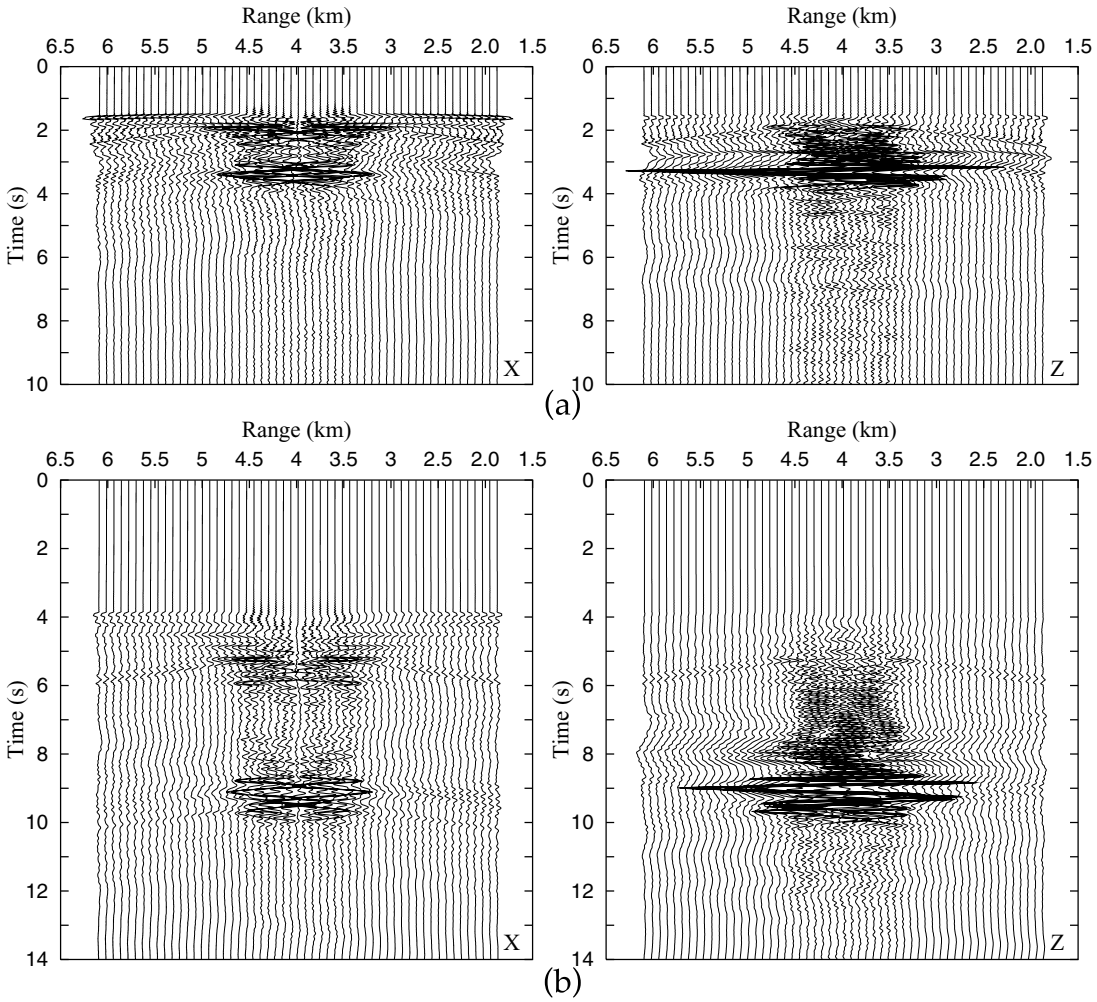

Figure 8. Time responses, with conversion to 3-D response, for lines of receivers crossing the fault zone illustrating the nature of the trapped wave system in the heterogeneous gouge zone (a) at $x = 8.59$ km (E_j in Fig. 5) and (b) at 16.88 km (K_j) from the source.

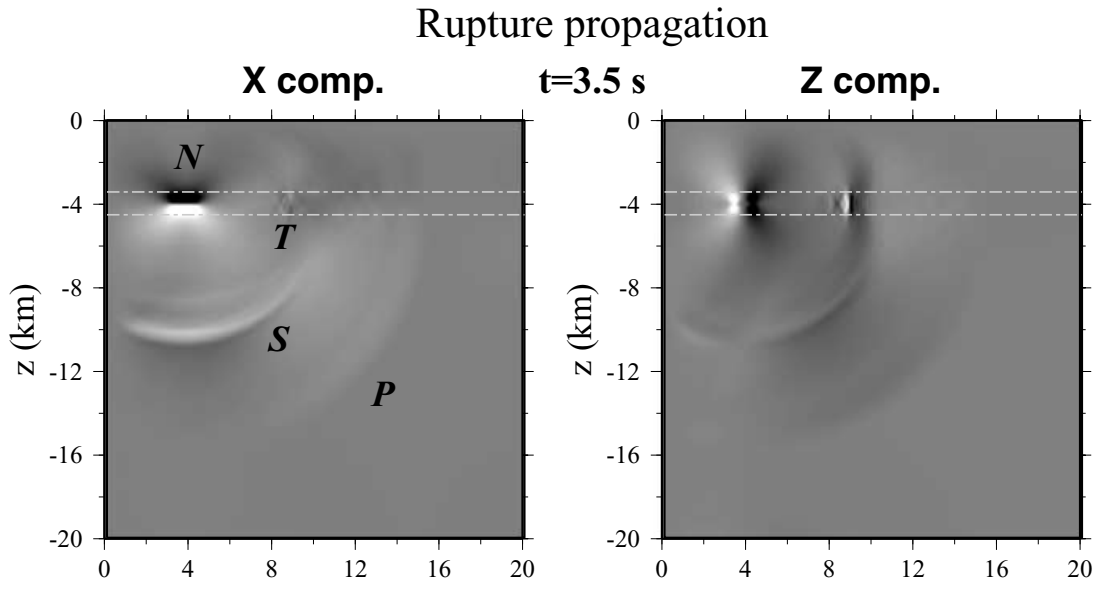

Figure 9. Snapshots of elastic wave propagation in a medium with a horizontal fault zone (Fig. 5) with a propagating 90° dip-slip rupture. The same magnitude of scalar moment M_0 as in Fig. 6 is considered, and subsequent dislocations are considered in an area with horizontal extent 0.86 km. The permanent displacement pattern on the x component displays a horizontally extended shape following the rupture direction, but that on the z component is concentrated at the ends of the rupture.

For realistic modelling, the source process needs to be considered and a direct representation of the faulting process is desired. In this section, we introduce a simple rupture-propagation problem in a fault zone by the superposition of multiple dislocation sources, each of which may have their own displacement time functions along the rupture-propagation direction in the fault zone. We consider once again the fault gouge zone model problem of Fig. 5 and consider a bilateral propagating rupture initiated at the same point as the line force location in Section 4.2. The rupture velocity is taken as 0.9 times the shear wave velocity (β_1) in the fault zone, and the rupture terminates at a distance 0.43 km (corresponding to five gridpoints) from the origin. Here we consider a simple case in which each segment of the fault has the same particle displacement time history (ramp model) and the same amount of energy release (i.e. the same permanent dislocation at steady state). However, the same approach can readily be extended to much more complex problems where every segment of the fault has own displacement time history and energy release rate.

For comparison with the results of the point-dislocation case (Section 4.2), we consider the same magnitude of seismic moment M_0 by distributing the magnitude evenly along the fault plane over the total rupture distance. The general character of the wavefields seen in the snapshots (Fig. 9) are similar to the point-dislocation case (Fig. 6). However, since the energy is released over a time interval at each segment of the fault, the transient waves exhibit smaller amplitudes and lower frequencies (see also, Fig. 10). Also, we note that there is now a much weaker *P* disturbance in the fault zone and consequently much fewer in the way of *S* head waves in the surroundings. The permanent displacement patterns (*N* in Fig. 9) around the fault display horizontal extension along the fault propagation direction

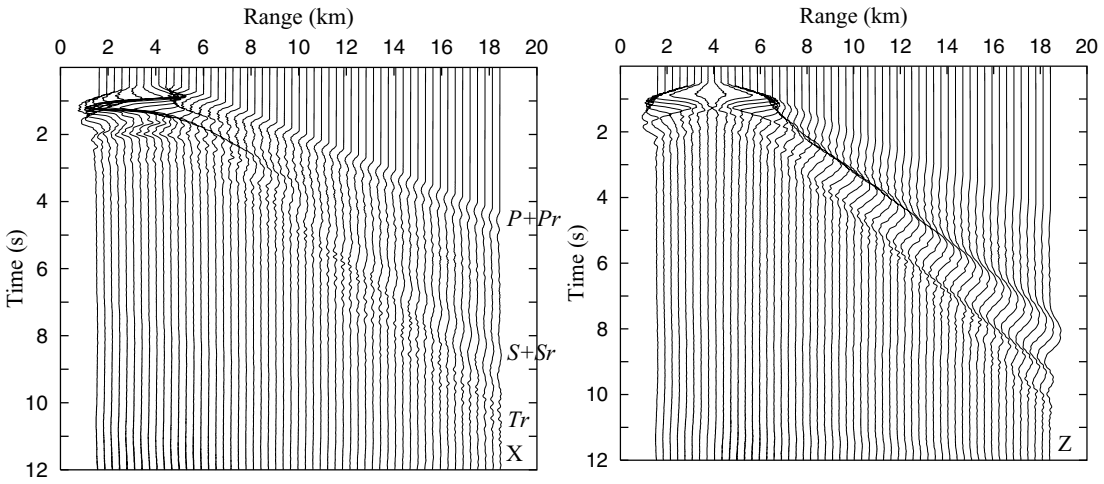

Figure 10. Time responses, with conversion to a 3-D response, for the propagating fault problem with 110 receivers placed at depths of $z = 5.5$ (a) and 16.9 km (b). the traces are amplified by a factor of 2 compared with Fig. 7. The main phases (*P, S, Pr, Sr, Tr*) are similar to those for a point dislocation but the frequency contents of phases are lower than those in Fig. 7, since the rupture velocity is lower than the elastic wave velocities.

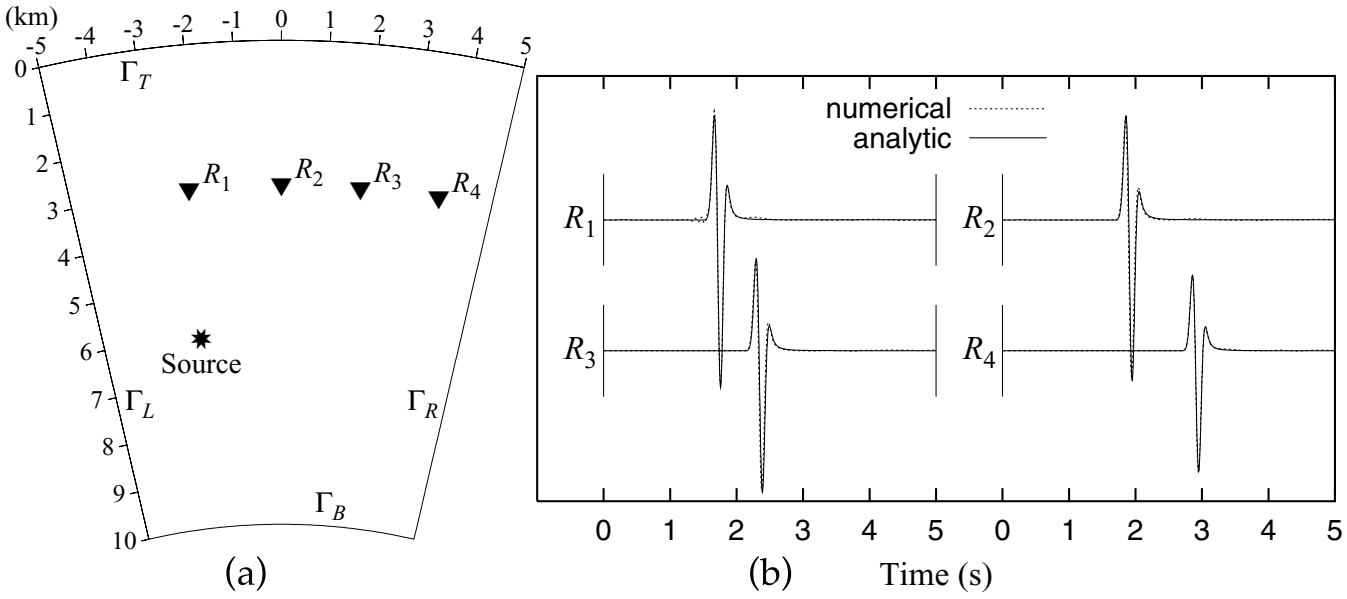

Figure 11. (a) Description of a homogeneous medium, part of the circle with radius 22 km, for a validation test of the wavelet-based method in circular media. Four receivers (R_j, $j = 1, 2, 3, 4$) are placed at a depth of 3.04 km and the source at a depth of 6.3 km. The four artificial boundaries (Γ_R, Γ_L, Γ_T, Γ_B) are treated as absorbing boundaries. (b) Comparisons between analytic solutions and numerical results recorded at the four receivers (R_j) in a homogeneous circular medium.

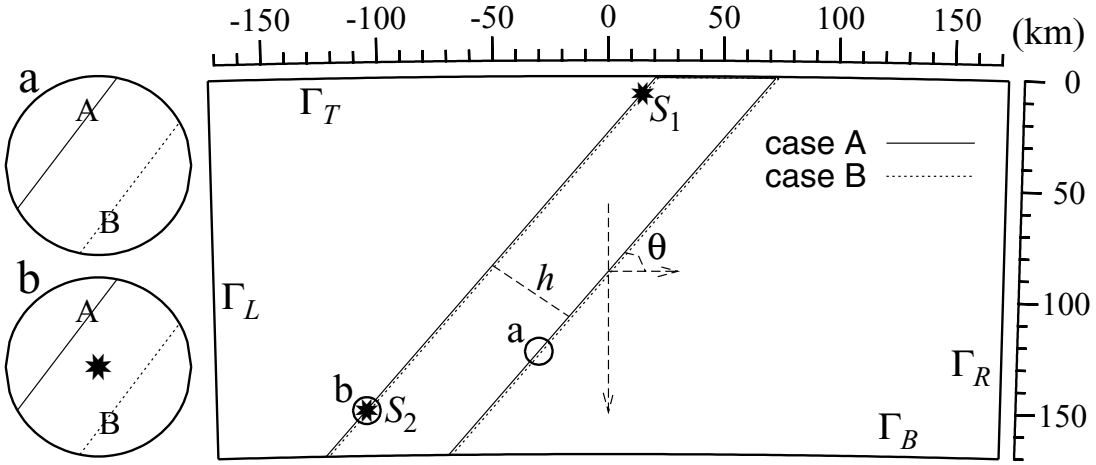

Figure 12. A simplified model of a subduction zone with a dip (θ) of 50°and a thickness (h) of 40 km. The uniform slab has a wave speed set 5 per cent higher than the wave speed just above the upper boundary and is embedded in the radially stratified model *ak135* (Kennett *et al.* 1995). Sources are placed at two representative depths: shallow (S_1, $z = 11.88$ km) and intermediate depth (S_2, $z = 149.15$ km). Point sources with a dominant frequency of 1 Hz are introduced near the boundaries of the slab. The four sources lie just below the upper boundary of the slab (case A), or just above the slab boundary (case B), and in a similar configuration just below the lower boundary (case C), or just above the boundary (case D).

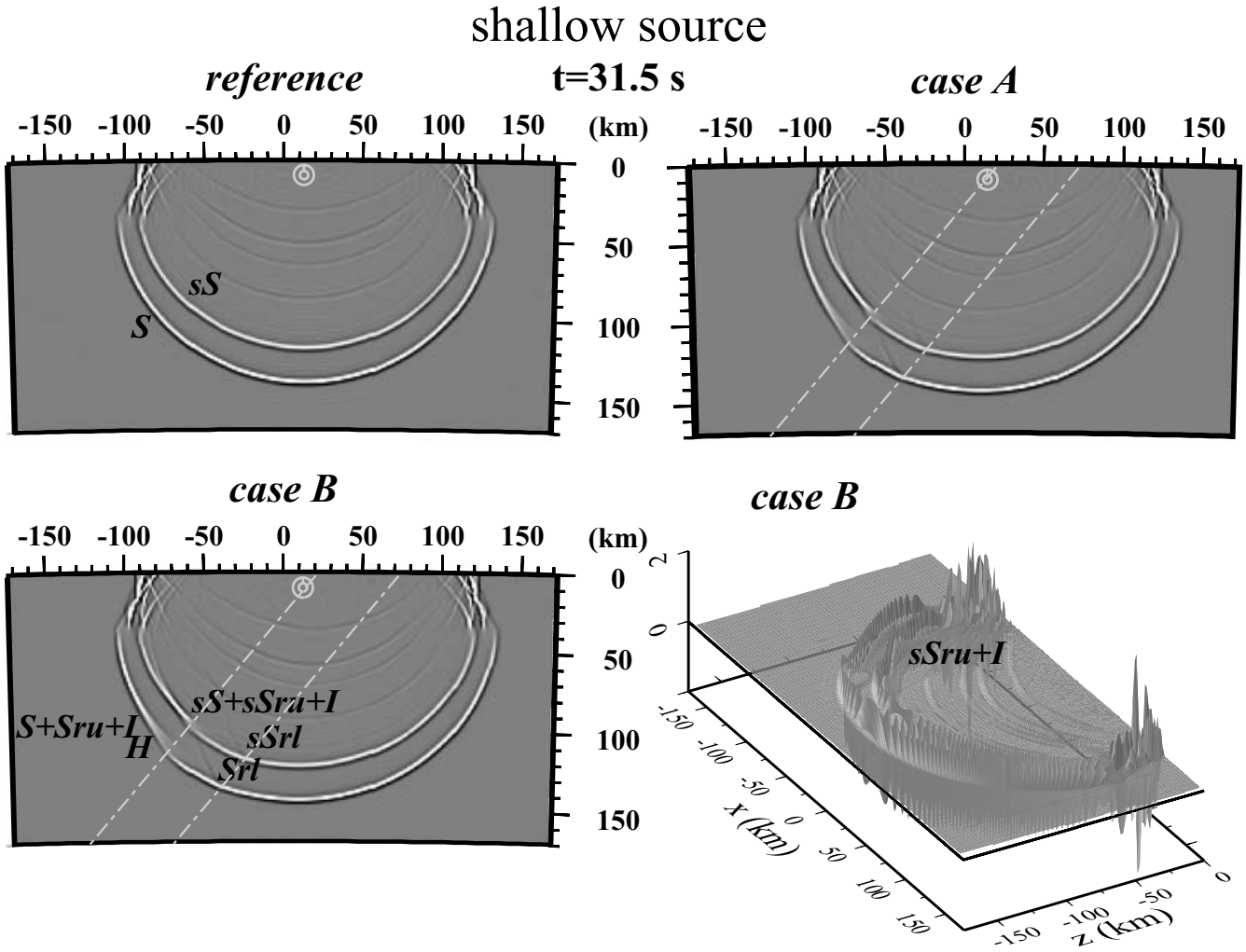

Figure 13. Snapshots of *SH*-wave propagation in the simplified subduction zone model with a shallow source at $t = 31.5$ s. Major phases in the reference model are direct waves (*S*), free-surface reflected waves (*sS*) and Love waves. The patterns of reflected waves at the upper boundary of the slab (*Sru, sSru*) and at the lower boundary (*Srl, sSrl*), depend on the source positions relative to the slab. Interface waves (*I*) and head waves (*H*) develop strongly along the slab boundary closest to the source.

in the x components. In contrast the permanent displacements are concentrated at the end of the rupture on the z component and are not discernible along the plane of rupture.

The time responses in Fig. 10 for the propagating rupture source are displayed with twice the amplification used in Fig. 7. The multiple reflected waves following S waves for receivers at short offset on the x components for the point dislocation case (Fig. 7) do not appear in the profiles for propagating rupture.

5 MODELLING IN SUBDUCTION ZONES

A further region in which sources occur within a zone of heterogeneity is in the coherent and systematic high-velocity zone of the subducting slab. The majority of earthquakes associated with the subduction zone lie within the slab but relatively close to its upper surface. Seismic waves generated from such sources within the slab have the potential of strong interaction with the slab boundaries with reflections and conversions. There is also the possibility of interface waves associated with the contrasts in properties at the edge of the slab. The combination of the effects introduced by the slab can have significant effects on the local wavefield and also have the potential to modify the high-frequency characteristics for teleseismic propagation.

Waveform and amplitude variations of incident waves propagating through a slab have been studied at regional distance with both numerical modelling (e.g. Cormier 1989; Sekiguchi 1992; Kennett & Furumura 2002) and observational analysis (Lay & Young 1989). Recently, waveguide effects in the accretionary prism above the slab have been investigated by Shapiro *et al.* (2000). However, the generation of secondary waves in subduction zones (such as reflected waves, interface waves) have not received much attention. Moreover, when waves interfere with a fast-velocity layer placed between low-velocity layers, it is possible to get tunnelling effects (Fuchs & Schulz 1976; Drijkoningen 1991), which depend on the frequency content of the wavefield and the thickness of the layer, which can contribute to waveform complexity. Thus, low-frequency waves with large wavelength are hardly affected by the presence of the subducting slab but the impact increases at higher frequencies.

We consider the *SH*-wave case at a regional scale, and show how the WBM method can be used to handle the presence of a simplified subduction zone embedded in a radially stratified background model, including secondary wave effects.

The subduction zone structure extends to such a depth that we cannot ignore the influence of the sphericity of the Earth and so need to adapt the WBM to a non-Cartesian coordinate system. Spherical finite-difference methods have been introduced for the simulation of *SH* waves in the mantle (Igel & Weber 1995; Chaljub & Tarantola 1997) and *P–SV* (Igel & Weber 1996) wave propagation in the sphere. An alternative approach, which remains in 2-D, was adopted by Furumura *et al.* (1998) with a cylindrical-coordinate

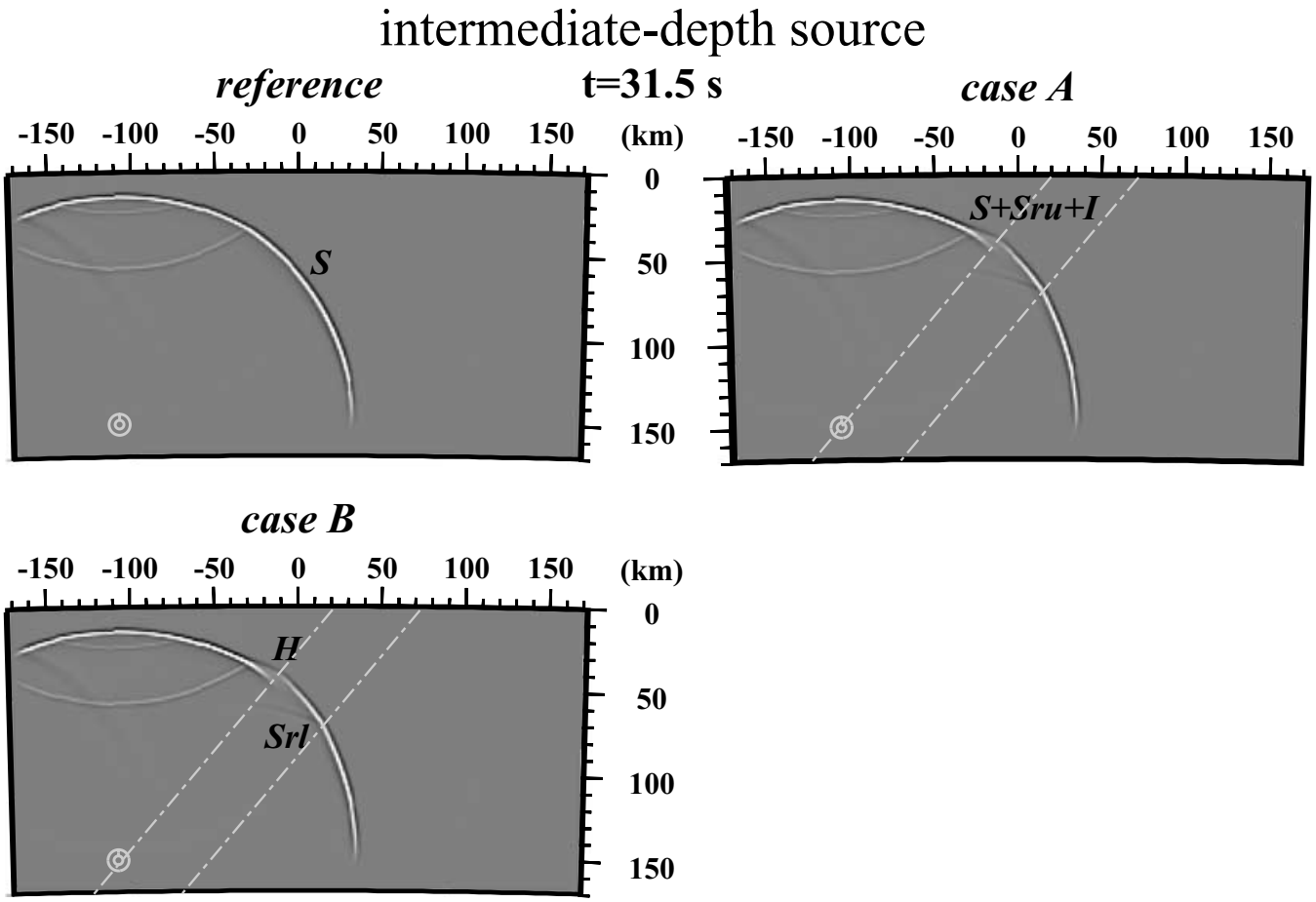

Figure 14. Snapshots of *SH*-wave propagation in subduction zones with an intermediate depth of source at $t = 31.5$s. The wavefields are simpler than those in Fig. 14, but the phases developing on boundaries are clearly shown to travel into the free surface. The main reflected waves (*Sru, Srl*), interface waves (*I*) and head waves (*H*) are indicated.

representation for *P–SV*-wave equations in modelling using a pseudospectral method. For a 2-D structure such as a subducting plate, modelling with a spherical coordinate system, requires the pole axis to be treated by a symmetry condition, with a vanishing displacement vector on the axis, and thus an additional boundary condition is needed. To preserve the simplicity of the situation we use cylindrical coordinates for *SH* waves with the background radially stratified model based on *ak135* (Kennett *et al.* 1995).

5.1 Numerical implementation

The *SH*-wave equation in a cylindrical coordinate (r, θ, y) system (*cf.* Aki & Richards 1980) takes the form

$$\frac{\partial^2 u_y}{\partial t^2} = \frac{1}{\rho}\left(\frac{\sigma_r}{r} + \frac{\partial \sigma_r}{\partial r} + \frac{1}{r}\frac{\partial \sigma_\theta}{\partial \theta} + f_y\right), \tag{12}$$

where the stress terms σ_r and σ_θ are given by

$$\sigma_r = \mu \frac{\partial u_y}{\partial r}, \quad \sigma_\theta = \frac{\mu}{r}\frac{\partial u_y}{\partial \theta}. \tag{13}$$

This set of equations for *SH* can be recast in the wavelet representation in a similar way to that in Sections 2 and 3, working with normalized radius.

The traction-free condition at the free surface and the core–mantle boundary (if applicable) is $\sigma_r = 0$, and this can be implemented via equivalent forces in **N**, eq. (5), as in Hong & Kennett (2002a).

5.2 Validation tests

The accuracy of the wavelet-based method in cylindrical coordinates has been tested with a variety of models where analytic solutions are available. We illustrate these tests for a cylinder with small radius where the influence of curvature is strong.

We consider a portion of a uniform cylinder with radius 22 km (Fig. 11a). Four artificial boundaries (Γ_R, Γ_L, Γ_T, Γ_B) are treated by absorbing boundary conditions. Four receivers (R_j, $j = 1, 2, 3, 4$) are placed at a depth of 3.04 km in a row with interval 1.61 km, and a point force is applied at a depth of 6.3 km. The numerical model is represented with 128×128 gridpoints, the shear wave velocity is set to be 2.0 km s^{-1}, and the density 2.2 Mg m^{-3}. A Ricker wavelet with dominant frequency 4.5 Hz is implemented for the source time function.

As shown in Fig. 11(b), the wavelet-based method generates time responses with correct traveltimes and amplitudes for this uniform cylinder case. A barely noticeable high-frequency jitter distinguishes the numerical simulation from the analytical results.

A similar comparison has been made for both the effects of the free surface and layering for model segments placed at the surface of the Earth so that curvature effects are minimized. The replication of the analytic results matches that of Fig. 11(b) and so confirms the accuracy of the cylindrical WBM method. For more complex stratified models analytic solutions are not available but a strong check on the validity of the WBM method is provided by the precise match of the wave front patterns for both shallow and deep sources.

5.3 *SH* waves in subduction zones

The geometry of subducting slabs is approximately 2-D, but the velocity anomalies revealed by seismic tomography indicate that there can be significant variations along a single subduction zone (e.g. Pankow & Lay 2002; Kennett 2002; Widiyantoro *et al.*1999; Ding & Grand 1994).

Here we implement a simplified slab model based on a recent study (Pankow & Lay 2002) of shear wave velocity structure in the Kurile subduction zone. We consider a slab with a dip (θ) of

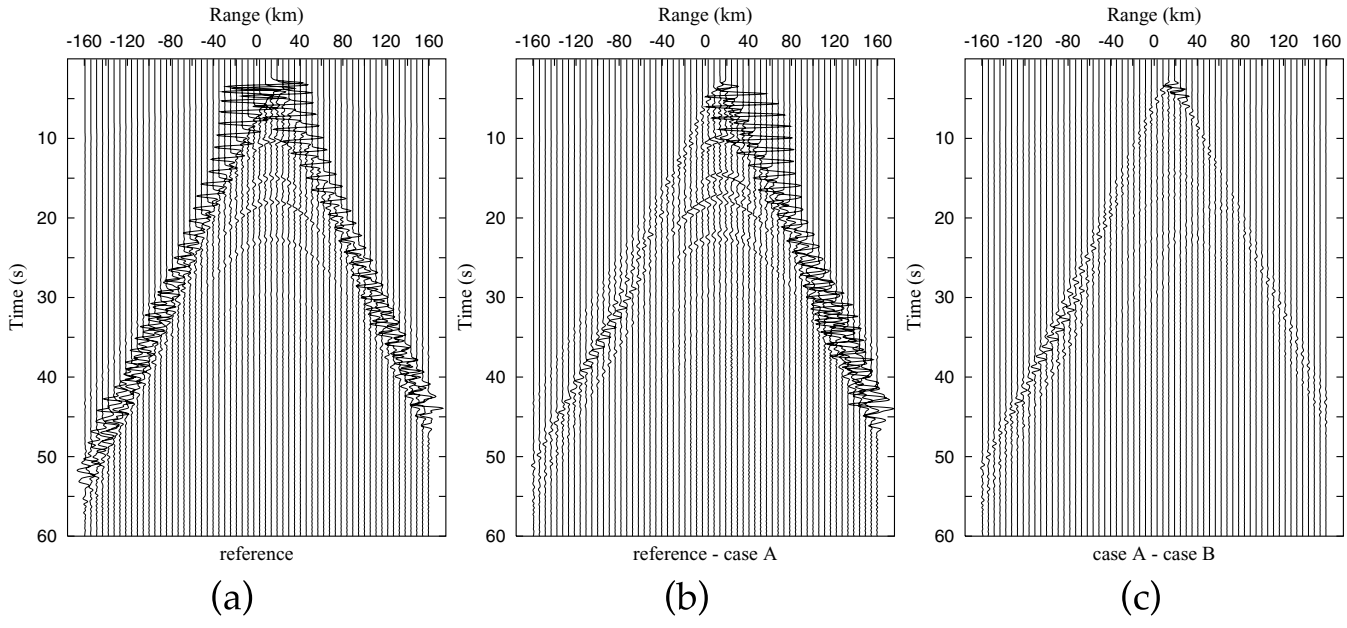

Figure 15. Seismograms at the surface for shallow sources in the simplified subduction model. (a) The main features of the seismograms are well represented by the reference model. The features associated with the presence of the slab are enhanced by considering difference seismograms. The main features of source positions at the upper and lower slab boundaries can be seen from (b) reference case A (upper), (c) reference case C (lower). The more subtle differences arising from the position of the source, inside or outside the slab, are apparent from the difference seismograms (d) case A–case B and (e) case C–case D. The main differences arise from the time advance of the waves in the slab models when they pass through the slab. Reflected arrivals from the upper boundary of the slab are important for sources near the upper boundary, and are more pronounced for case B where the source lies outside the slab.

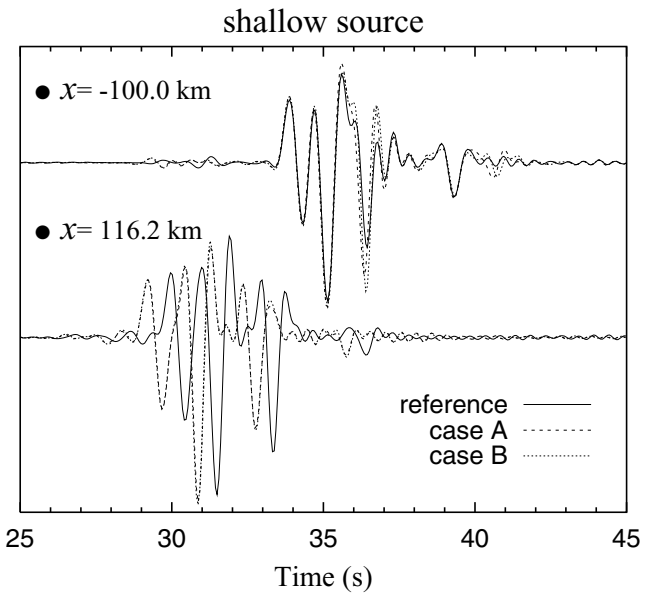

Figure 16. Comparisons among time responses of models for shallow sources at two representative places ($x = -100$, 116.2 km): among (a) reference model, cases A and B and (b) reference model, cases C and D. The strong influence of passage through the slab is apparent in each case.

50° and a velocity anomaly raised by 5 per cent compared with its surroundings (Fig. 12); the properties of the slab are constant across its thickness. The slab is embedded in the radially stratified model *ak135* (Kennett *et al.* 1995). The thickness (h) of the slab is taken as 40 km and the velocity anomaly of the slab starts at 0.68 km depth. Two different positions of the source relative to the slab are considered for both a shallow source (S_1 in the figure, $z = 11.88$ km) and an intermediate depth source (S_2, $z = 149.15$ km) depths. The two sources lie just below the upper boundary of the slab (case A), or just above the slab boundary (case B). Here, the slab model in case B is generated by a rotation of case A clockwise about the centre of the Earth by 1.35 km.

The source location is kept fixed so that direct comparison of the seismograms can be made for free surface receivers. The source time function is taken as a Ricker wavelet with a dominant frequency of 1 Hz. The domain is represented with 512 ×256 gridpoints; three domain boundaries ($\Gamma_R, \Gamma_L, \Gamma_B$) are treated by absorbing boundary conditions, and the top domain boundary (Γ_T) is considered as a free surface. We consider a slab with a constant relative velocity anomaly as a means of understanding the effects of slab boundaries on the waveforms and the systematic deformation of wave fronts due to subduction zones.

Figs 13 and 14 compare snapshots for the two source positions at $t = 31.5$ s for shallow source depths and intermediate depth of source. The reference snapshot in the figure is computed in the radially stratified Earth model *ak135*. The outlines of the perturbed slab are superimposed on the snapshots to aid in identification of the different classes of arrivals.

For shallow sources (S_1), significant interface waves (I) and reflected waves (*Sru*, *sSru*) propagate along the upper boundary and are mixed in with or follow both the *S* and *sS* phases. Weak reflected waves (*Srl, sSrl*) can be recognized from their hook shape. The interface waves (I) and reflected waves (*sSru*) following *sS* waves are shown clearly in the 3-D perspective view, the last snapshot, in the figure. Also, head wave effects outside the slab (H) are apparent since they become detached from reflected waves with both distance and time (see, H in case B). We note that, when sources are located around the lower boundary of the slab, head waves have a less distinct identity (this figure has not been provided).

For the group of intermediate-depth sources (Fig. 14) the wave front patterns are relatively simple and the effects of the slab can be transferred updip towards the surface. Noticeable reflected waves and interface waves develop along the boundary near the source, and weak reflected waves are generated at the other boundary of the slab. Head waves surrounding the slab appear in each case.

The influence of the high-velocity slab can be clearly seen in the seismograms recorded at the surface. We use a set of 60 receivers with a spacing of 5.4 km, and enhance the various arrivals associated with the presence of the slab by using difference seismograms between the difference cases. In Fig. 15 we show the seismograms for a shallow source for the reference model and the difference seismograms between cases A, B and the reference model. The general pattern of the wave trains for the reference case is preserved in all cases, but the introduction of a slab leads to traveltime anomalies that depend on the relative positions of receivers to the source and the slab. The main variations occur on the far side of the slab from the source position as can be seen in the difference seismograms (Fig. 15b), the strong contributions arise from the phase shifts induced by the passage through the slab.

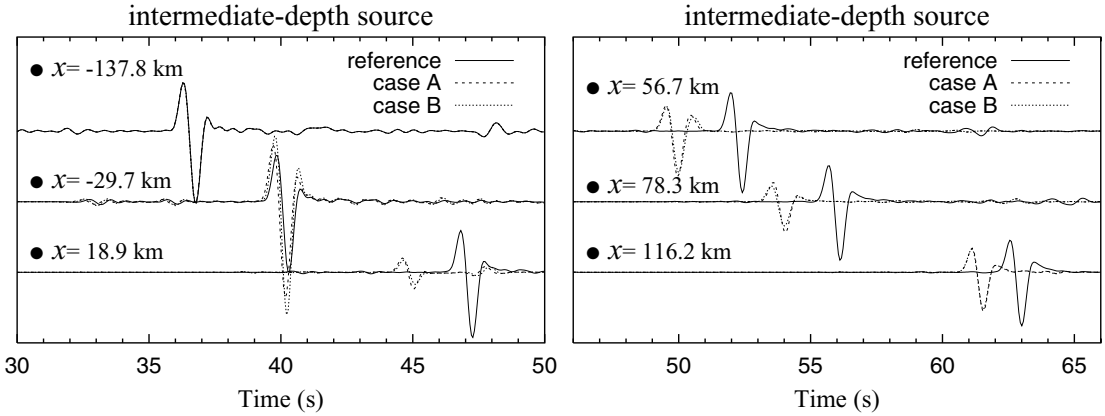

Figure 17. Comparisons of seismograms for intermediate-depth sources at six representative locations ($x = -137.8$, -29.7, 18.9, 56.7, 78.3, 116.2km): (a) reference model, cases A and B; (b) reference model, cases C and D. Both amplitude differences and traveltime anomalies are displayed in traces with characteristic patterns depending on the configuration of the source relative to the slab.

Reflected waves from the upper boundary of the slab also play an important role in the waveform variation in the later part of the wave trains recorded above the slab in a narrow interval $x = -60$ to -140 km, Fig. 15(b), corresponding to ranges of 80–160 km from the epicentre. For the source inside the slab (case A) the reflected waves are mainly generated by *sS* waves, but for an external source (case B) both *S* and *sS* waves contribute and the amplitude is enhanced (see Figs 15b and c for $x = -100.0$ km).

The waveforms for a shallow source at two locations are compared in Fig. 16. At $x = -100$ km, the influence of the reflected waves for the upper boundary of the slab can be seen in the modification of the later part of the main pulse. With the observation point on the other side of the slab at $x = 116.2$ km, there is a bulk shift of the waveforms.

For an intermediate depth source a rather different pattern of arrivals is produced. Although the slab offers a fast propagation path, energy is continuously shed from the high-velocity slab into the lower-velocity surroundings (note the weakened wave fronts in the slab in Fig. 14). As a result the waves emerging at the surface in the slab zone are advanced in time but show rather small amplitudes compared with the reference case (Fig. 17 at $x = 18.9$ km). Direct transmission through the slab also induces some loss in amplitude due to the contrasts at the slab boundaries (at $x = 78.3$, 116.2 km). Reflected waves can contribute to local enhancement of the amplitude just outside the slab zone ($x = -29.7$ km).

6 DISCUSSION AND CONCLUSIONS

The wavelet-based method (WBM) provides an effective means of simulating elastic wave propagation in heterogeneous media, since it can cope with rapid variations in physical properties without loss of accuracy. With the improved scheme for source representation introduced in this paper it is possible to place moment-tensor or dislocation sources directly in regions of heterogeneity. This enables the WBM to be used effectively in a variety of problems where significant contrasts in physical properties occur in the neighbourhood of the source.

In the case of sources within a highly heterogeneous fault gouge zone, we get strong waveguide effects for *P–SV* waves, which are modified somewhat when we introduce a propagating rupture. The fault-trapped waves decay outside the fault zone and the presence of high-frequency energy provides a good guide to the location of the fault zone itself.

In subduction zones, the slab represents a region of elevated wave speed compared with its surroundings. Although propagation along the slab is fast, substantial energy is shed in an antiwaveguide effect. The contrasts at the boundaries of the slab have the potential to generate reflected and interface phases that can add to the complexity of the seismograms for stations in the vicinity of the slab.

ACKNOWLEDGMENTS

This paper has benefited from the helpful review comments of Drs Yong-Gang Li, Heiner Igel and Michael Korn (editor). Also, we thank the Australian National University Supercomputer Facility for allocation of computer time on the Alpha server.

REFERENCES

Aki, K. & Richards, P.G., 1980. *Quantitative Seismology, Theory and Methods,* Vol. 1, Freeman, San Francisco.

Alterman, Z. & Karal, F.C., Jr, 1968. Propagation of elastic waves in layered media by finite difference methods, *Bull. seism. Soc. Am.,* **58,** 367–398.

Ben-Menahem, A. & Singh, S.J., 1981. *Seismic Waves and Sources,* Springer-Verlag, New York.

Ben-Zion, Y., 1998. Properties of seismic fault zone waves and their utility for imaging low-velocity structures, *J. geophys. Res.,* **103,** 12 567–12 585.

Ben-Zion, Y. & Aki, K., 1990. Seismic radiation from an *SH* line source in a laterally heterogeneous planar fault zone, *Bull. seism. Soc. Am.,* **80,** 971–994.

Beylkin, G., 1992. On the representation of operators in bases of compactly supported wavelets, *SIAM J. Numer. Anal.,* **6,** 1716–1740.

Beylkin, G. & Keiser, J.M., 1997. On the adaptive numerical solution of nonlinear partial differential equations in wavelet bases, *J. Comput. Phys.,* **132,** 233–259.

Chaljub, E. & Tarantola, A., 1997. Sensitivity of *SS* precursors to topography on the upper-mantle 660-km discontinuity, *Geophys. Res. Lett.,* **24,** 2613–2616.

Cormier, V.F., 1989. Slab diffraction of *S* waves, *J. geophys. Res.,* **94,** 3006–3024.

Coutant, O., Virieux, J. & Zollo, A., 1995. Numerical source implementation in a 2-D finite difference scheme, *Bull. seism. Soc. Am.,* **85,** 1507–1512.

Ding, X.-Y. & Grand, S.P., 1994. Seismic structure of the deep kurile subduction zone, *J. Geophys. Res.,* **99**(B12), **23,** 767–786.

Drijkoningen, G.G., 1991. Tunnelling and the generalized ray method in piecewise homogeneous media, *Geophys. Prospect.,* **39,** 757–781.

Falk, J., Tessmer, E. & Gajewski, D., 1998. Efficient finie-difference modelling of seismic waves using locally adjustable time steps, *Geophys. Prospect.,* **46,** 603–616.

Fuchs, K. & Schulz, K., 1976. Tunneling of low-frequency waves through the subcrustal lithosphere, *J. Geophys.,* **42,** 175–190.

Furumura, T. & Kennett, B.L.N., 1998. On the nature of regional seismic phases—III. The influence of crustal heterogeneity on the wavefield for subduction earthquakes: the 1985 Michoacan and 1995 Copala, Guerrero, Mexico earthquakes, *Geophys. J. Int.,* **135,** 1060–1084.

Furumura, T., Kennett, B.L.N. & Furumura, M., 1998. Seismic wavefield calculation for laterally heterogeneous whole Earth models using the pseudospectral method, *Geophys. J. Int.,* **135,** 845–860.

Graves, R.W., 1996. Simulating seismc wave propagation in 3-D elastic media using staggered-grid finite differences, *Bull. seism. Soc. Am.,* **86,** 1091–1106.

Hong, T.-K. & Kennett, B.L.N., 2002a. A wavelet-based method for simulation of two-dimensional elastic wave propagation, *Geophys. J. Int.,* **150,** 610–638.

Hong, T.-K. & Kennett, B.L.N., 2002b. On a wavelet-based method for the numerical simulation of wave propagation, *J. Comput. Phys.,* **183,** 577–622.

Hong, T.-K. & Kennett, B.L.N., 2003. Scattering attenuation of 2D elastic waves: theory and numerical modeling using a wavelet-based method, *Bull. seism. Soc. Am.,* **93,** 922–938.

Hough, S.E., Ben-Zion, Y. & Leary, P., 1994. Fault-zone waves observed at the Southern Joshua Tree earthquake rupture zone, *Bull. seism. Soc. Am.,* **84,** 761–767.

Huang, B.-S., Teng, T.-L. & Yeh, Y.T., 1995. Numerical modeling of fault-zone trapped waves: acoustic case, *Bull. seism. Soc. Am.,* **85,** 1711–1717.

Igel, H., Mora, P. & Riollet, B., 1995. Anisotropic wave propagation through finite-difference grids, *Geophysics,* **60,** 1203–1216.

Igel, H., Ben-Zion, Y. & Leary, P.C., 1997. Simulation of *SH*- and P–SV-wave propagation in fault zones, *Geophys. J. Int.,* **128,** 533–546.

Igel, H., Jahnke, G. & Ben-Zion, Y., 2002. Numerical simulation of fault zone guided waves: accuracy and 3-D effects, *Pure appl. Geophys.,* **159,** 2067–2083.

Igel, H. & Weber, M., 1995. *SH*–wave propagation in the whole mantle using high-order finite differences, *Geophys. Res. Lett.,* **22,** 731–734.

Igel, H. & Weber, M., 1996. *P–SV*–wave propagation in the Earth's mantle using finite differences: applications to heterogeneous lowermost mantle structure, *Geophys. Res. Lett.,* **23,** 415–418.

Jahnke, G., Igel, H. & Ben-Zion, Y., 2002. Three-dimensional calculations of fault-zone-guided waves in various irregular structures, *Geophys. J. Int.,* **151,** 416–426.

Kasahara, K., 1981. *Earthquake Mechancis,* Cambridge University Press, Cambridge.

Käser, M. & Igel, H., 2001. Numerical simulation of 2-D wave propagation on unstructured grids using explicit differential operators, *Geophys. Prospect.,* **49,** 607–619.

Kelly, K.R., Ward, R.W., Treitel, S. & Alford, R.M., 1976. Synthetic sismograms: a finite-difference approach, *Geophysics,* **41,** 2–27.

Kennett, B.L.N., 2001. *Seismic Wavefield*, vol. I:*Introduction and Theoretical Development,* p. 370, Cambridge University Press, New York.

Kennett, B.L.N., 2002. *Seismic Wavefield,* vol. II: *Interpretation of Seismograms on Regional and Global Scales,* p. 534, Cambridge University Press, New York.

Kennett, B.L.N. & Furumura, T., 2002. The influence of 3-D structure on the propagation of seismic waves away from earthquakes, *Pure appl. Geophys.,* **159,** 2113–2131.

Kennett, B.L.N., Engdahl, E.R. & Buland, R., 1995. Constraints on seismic velocities in the Earth from travel times, *Geophys. J. Int.,* **122,** 108–124.

Komatitsch, D. & Tromp, J., 2002. Spectral-element simulations of global seismic wave propagation—I. Validation, *Geophys. J. Int.,* **149,** 390–412.

Kosloff, D., Reshef, M. & Loewenthal, D., 1984. Elastic wave calcuations by the Fourier method, *Bull. seism. Soc. Am.,* **74,** 875–891.

Kosloff, D., Kessler, D., Filho, A.Q., Tessmer, E., Behle, A. & Strahilevitz, R., 1990. Solution of the equations of dynamic elasticity by a Chebychev spectral method, *Geophysics,* **55,** 734–748.

Lay, T. & Wallace, T.C., 1995. *Modern Global Seismology,* Academic, New York.

Lay, T. & Young, C.J., 1989. Waveform complexity in teleseismic broadband *SH* displacements: slab diffractions or deep mantle reflections?, *Geophys. Res. Lett.,* **16,** 605–608.

Levander, A.R., 1988. Fourth-order finite-difference P–SV seismograms, *Geophysics,* **53,** 1425–1436.

Li, Y.-G., 1988. Trapped modes in a transversely isotropic fault-zone, *PhD thesis*, pp. 168–189, University of Southern California.

Li, Y.-G. & Leary, P.C., 1990. Fault zone trapped seismic waves, *Bull. seism. Soc. Am.,* **80,** 1245–1271.

Li, Y.-G. & Vidale, J.E., 1996. Low-velocity fault-zone guided waves: numerical investigations of trapping efficiency, *Bull. seism. Soc. Am.,* **86,** 371–378.

Li, Y.-G., Leary, P.C., Aki, K. & Malin, P.E., 1990. Seismic trapped modes in the Oroville and San Andreas fault zones, *Science,* **249,** 763–766.

Li, Y.-G., Aki, K., Vidale, J.E. & Xu, F., 1999. Shallow structure of the Landers fault zone from explosion-generated trapped waves, *J. geophys. Res.,* **104,** 20 257–20 275.

Li, Y.-G., M., Vidale, J.E., Day, S.M., Oglesby, D.D. & the SCEC Field Working Team, 2002. Study of the 1999 *M* 7.1 Hector mine, California, earthquake fault plane by trapped waves, *Bull. seism. Soc. Am.,* **92,** 1318–1332.

Pankow, K.L. & Lay, T., 2002. Modeling, *S* wave amplitude patterns for events in the Kurile slab using three-dimensional Gaussian beams, *J. geophys. Res.,* **107,** 10.1029/2001JB000594.

Roth, M. & Korn, M., 1993. Single scattering theory versus numerical modelling in 2-D random media, *Geophys. J. Int.,* **112,** 124–140.

Sato, H. & Fehler, M.C., 1998. *Seismic Wave Propagation and Scattering in the Heterogeneous Earth,* Springer-Verlag, New York.

Sekiguchi, S., 1992. Amplitude distribution of seismic waves for laterally heterogeneous structures including a subducting slab, *Geophys. J. Int.,* **111,** 448–464.

Shapiro, N.M., Olsen, K.B. & Singh, S.K., 2000. Wave-guide effects in subduction zones: evidence from three-dimensional modeling, *Geophys. Res. Lett.,* **27,** 433–436.

Vidale, J.E., 1987. Waveform effects of a high-velocity, subducted slab, *Geophys. Res. Lett.,* **15,** 542–545.

Vidale, J., Helmberger, D.V. & Clayton, R.W., 1985. Finite-difference seismograms for *SH* waves, *Bull. seism. Soc. Am.,* **75,** 1765–1782.

Widiyantoro, S., Kennett, B.L.N. & van der Hilst, R.D., 1999. Seismic tomography with *P* and *S* data reveals lateral variations in the rigidity of deep slabs, *Earth planet. Sci. Lett.,* **173,** 91–100.

Yomogida, K. & Etgen, J.T., 1993. 3-D wave propagation in the Los Angeles Basin for the Whittier–Narrows earthquake, *Bull. seism. Soc. Am.,* **83,** 1325–1344.